



Mid-infrared Studies of HD 113766 and HD 172555: Assessing Variability in the Terrestrial Zone of Young Exoplanetary Systems

Kate Y. L. Su¹, George H. Rieke¹, Carl Melis², Alan P. Jackson^{3,4}, Paul S. Smith¹, Huan Y. A. Meng¹, and András Gáspár¹

¹ Steward Observatory, University of Arizona, 933 N. Cherry Avenue, Tucson, AZ 85721, USA; ksu@as.arizona.edu

² Center for Astrophysics and Space Sciences, University of California, San Diego, CA 92093, USA

³ Center for Planetary Sciences, University of Toronto at Scarborough, 1265 Military Trail, Toronto, ON M1C 1A4, Canada

⁴ School of Earth and Space Exploration, Arizona State University, 781 E. Terrace Mall, Tempe, AZ 85287, USA

Received 2020 May 4; revised 2020 June 3; accepted 2020 June 11; published 2020 July 20

Abstract

We present multiepoch infrared photometry and spectroscopy obtained with warm Spitzer, Subaru, and the Stratospheric Observatory for Infrared Astronomy to assess variability for the young (~ 20 Myr) and dusty debris systems around HD 172555 and HD 113766A. No variations (within 0.5%) were found for the former at either 3.6 or 4.5 μm , while significant nonperiodic variations (peak to peak of $\sim 10\%$ – 15% relative to the primary star) were detected for the latter. Relative to the Spitzer Infrared Spectrograph spectra taken in 2004, multiepoch mid-infrared spectra reveal no change in either the shape of the prominent 10 μm solid-state features or the overall flux levels (no more than 20%) for both systems, corroborating the fact that the population of submicron-size grains that produce the pronounced solid-state features is stable over a decadal timescale. We suggest that these submicron-size grains were initially generated in an optically thick clump of debris of millimeter-size vapor condensates resulting from a recent violent impact between large asteroidal or planetary bodies. Because of the shielding from the stellar photons provided by this clump, intense collisions led to an overproduction of fine grains that would otherwise be ejected from the system by radiation pressure. As the clump is sheared by its orbital motion and becomes optically thin, a population of very fine grains could remain in stable orbits until Poynting–Robertson drag slowly spirals them into the star. We further suggest that the 3–5 μm disk variation around HD 113766A is consistent with a clump/arc of such fine grains on a modestly eccentric orbit in its terrestrial zone.

Unified Astronomy Thesaurus concepts: Circumstellar matter (241); Debris disks (363); Exozodiacal dust (500); Infrared excess (788); Early-type stars (430); Extrasolar rocky planets (511)

Supporting material: machine-readable table

1. Introduction

Small bodies in our solar system like asteroids, Kuiper-belt objects, and comets are the leftovers and fragments of planetesimals that failed to form planets. These bodies are known to be present around stars from the detection of circumstellar dust known as debris disks, which are created as these planetesimals are destroyed. Debris disks offer the opportunity to characterize planetary systems and their evolution from when they emerge from protoplanetary disks into old age (Wyatt 2008; Krivov 2010; Matthews et al. 2014; Hughes et al. 2018). These gas-poor disks are composed of dust grains ranging upward in size from $\lesssim 1 \mu\text{m}$, which are continually replenished by sublimation and collisions of parent bodies as the byproduct of planet formation. Sensitive infrared surveys with space telescopes (e.g., IRAS, Spitzer, Herschel, and Wide-field Infrared Survey Explorer (WISE)) have identified thousands of debris disks around mature stars through measurement of the infrared signal when this dust is heated. These observations trace a pattern of development thought to be similar to that of the solar system (Chen et al. 2020). Common features, such as the coexistence of warm (~ 150 K) and cold (~ 50 K) dust, suggest underlying order in debris disk structures and illuminate various processes about the formation and evolution of exoplanetary systems (Su & Rieke 2014).

A small percentage of stars just beyond the epoch of natal gas-rich disk dispersal show extremely large infrared excesses (Balog et al. 2009; Kennedy & Wyatt 2013; Meng et al. 2017). These systems have hot ($\gtrsim 300$ K) terrestrial zone dust levels

sufficient to intercept 1%–10% of the star’s light and thermally reemit it in the mid-infrared. The ages of these extreme systems tend to be between 10 and 200 Myr, so the dust is commonly interpreted as the product of terrestrial planet formation (e.g., Melis et al. 2010, 2013; Meng et al. 2014). In this scenario, the high dust levels originate in giant impacts analogous to the event that formed the Earth–Moon system (e.g., Jackson & Wyatt 2012). However, this interpretation is not unique (e.g., Melis 2016). An alternative possibility is that the high dust levels result from transient dynamical clearing after the gas dispersal of regions inhabited by planetesimals, most likely due to the enhanced excitation from adjacent large bodies such as planets. This mechanism might have operated in the past for the outer asteroid belt due to its close proximity to Jupiter (Liou & Malhotra 1997). A third possibility, under appropriate conditions applicable for a massive belt of planetesimals around young early-type stars, is preservation of a population of fine grains that traditionally would have been thought to have been blown out of the system on short timescales (Thebault & Kral 2019).

In some systems, it has been discovered that the hot dust emission can be highly variable, supporting the terrestrial planet formation hypothesis. The variability provides a unique opportunity to learn about these events and their roles in terrestrial planet formation (Melis et al. 2012). Successful models to explain these infrared light curves can extract very diagnostic information about the violent collisions such as the

impact time, location, and the dominant sizes of the resulting fragments (Su et al. 2019). To gain a broader insight into the behavior of these extreme debris disks requires that we understand individual systems, including how rapidly the resulting infrared excess rises and fades and which part of the disk is responsible for any variability.

Here we report multiepoch, mid-infrared observations of two young debris disks around HD 113766A and HD 172555 to search for infrared variability. Both stars are well-studied infrared-excess systems that exhibit prominent solid-state features in the mid-infrared, indicative of abundant submicron-size grains. HD 113766 is a binary system with a projected separation of $1''4$ (Holden 1976; Fabricius & Makarov 2000). Only the primary (HD 113766A) has infrared excess (i.e., a debris disk; Meyer et al. 2001). Spectra of the combined system indicate a type of F2V (Pecaut et al. 2012; obtained with a $2''0$ slit), while the spectrum of component B, which is ~ 0.3 mag fainter at V , indicates it is F6V (Chen et al. 2011). This star belongs to the Lower Centaurus-Crux subgroups of the Scorpius–Centaurus OB association and hence is ~ 17 Myr of age (Pecaut et al. 2012). HD 172555 is an A7V star, in the ~ 20 Myr old β Pic moving group (Mamajek & Bell 2014). It is also a binary, but the low-mass companion is at least 2000 au away (Torres et al. 2006) and has no infrared excess (Rebull et al. 2008; Riviere-Marichalar et al. 2014). Although both systems are at a similar age, HD 113766A is much dustier than HD 172555, with an infrared fractional luminosity ($f_d = L_{\text{IR}}/L_*$) of $\sim 2 \times 10^{-2}$ for the former and $\sim 7 \times 10^{-4}$ for the latter (Mittal et al. 2015).

Observations used in this work are reported in Section 2, including new photometry obtained during the warm Spitzer mission and mid-infrared spectroscopy obtained with the Stratospheric Observatory for Infrared Astronomy (SOFIA) and Subaru. We also review all existing infrared observations (published and unpublished) to assess disk variability. We find significant variations in the hot dust around HD 113766A. However, we find that the flux from HD 172555 is dominated by the output of the stellar photosphere at 3.6 and 4.5 μm , which shows no variations in our data. In Section 3, we discuss the disk structures inferred from spectral energy distribution (SED) models and spatially resolved images to analyze the implications of the observed variability. The conclusions are given in Section 4.

2. Observations and Results

2.1. Warm Spitzer/IRAC

Multiple Infrared Array Camera (IRAC) 3.6 and 4.5 μm observations were obtained during the Spitzer warm mission, resulting in a total of 11 Astronomical Observation Requests (AORs) for HD 172555 from PID 90250 (PI: Stapelfeldt) and 11093 (PI: Su), and 67 AORs for HD 113766 from PID 11093. Observations for HD 172555 were performed using the subarray mode to avoid saturation and a frame time of 0.02 s in a four-point Gaussian dither pattern with medium scale. Only 3.6 μm data were obtained under PID 90250, but both the 3.6 and 4.5 μm bands were used under PID 11093. For HD 113766, the full array mode with a frame time of 0.4 s and 10 point cycling dither pattern in medium scale were used. Both objects have two Spitzer visibility windows per year with each having a length of ~ 46 –52 days. Various observation cadences were used to search for flux variability. A cadence of 10 ± 2

days was used for HD 172555 under PID 11093 for both visibility windows in 2016, where the flux can be compared to the one obtained in 2013 under PID 90250. For HD 113766, 5 ± 2 and 15 ± 2 days were used in individual visibility windows. Details about the observations (AOR Keys, observed date, and time) are given in Tables A1 and A2.

These data were first processed by the Spitzer Science Center with the IRAC pipeline S19.2.0. We then performed aperture photometry on the basic calibrated data images following the procedure outlined in Meng et al. (2015) for both full and subarray data. The resultant photometry is also given in Tables A1 and A2. The Spitzer photometry includes contributions from both the star and the dust emission around it.

For HD 172555, we used an aperture 3 pixels in radius and a sky annulus between radii of 12 and 20 pixels (pixel scale of $1''22$) with aperture correction factors of 1.112 and 1.113 for 3.6 and 4.5 μm , respectively. No variability was found within 0.5% rms in either band between 2013 and 2017. The measurements are also consistent with the expected stellar photosphere (i.e., no infrared excess within a few percent of the stellar photospheric model at these wavelengths). Limited by the optical and near-infrared measurements, the photospheric prediction using stellar models is typically as good as a few percent. We therefore verified the non-infrared excess by comparing signals in the two IRAC bands. Because any residual dust is likely to be at a temperature of ~ 300 –400 K (Lisse et al. 2009), it would contribute more flux to the 4.5 μm band than the 3.6 μm band. However, allowing for the expected color difference between A0V and A7V, the observed fluxes in those bands agree with expectations for the stellar photosphere alone (Bohlin et al. 2011) to within 1.5%.

For simplicity, when we refer to the HD 113766 system hereafter, we mean the planetary system around the primary. Because the binary is not completely resolved in the IRAC observations, we used an aperture of 5 pixels ($6''1$) with a sky annulus of 12–20 pixels ($14''6$ – $24''5$) to measure the photometry and ensure the flux from both stars is within the aperture. As shown in Table A1, there is $\sim 5\%$ – 8% peak-to-peak variability in the measured total fluxes at both bands.

We determined the observational repeatability by assessing the photometry of field stars in the data. Unfortunately, there is no star within the field of view that is as bright as HD 113766. For fainter field stars (by more than a factor of 10), $\lesssim 2\%$ repeatability is found at both bands. We conclude that the data on HD 113766 have $\sim 1\%$ repeatability, similar to other high signal-to-noise measurements obtained in the same program (e.g., Su et al. 2019). This suggests that the 5%–8% variability is significant. The optical photometry (in both V and g bands) from the All Sky Automated Survey for SuperNovae network (Kochanek et al. 2017) suggests that the unresolved binary has a combined stellar output stable within 1%, indicating that the variability comes from the disk around the primary. We determined the combined stellar output to be 728 and 456 mJy in the 3.6 and 4.5 μm bands, respectively (see Appendix B for details). The time-series disk fluxes (at both bands) after subtracting the stellar components and the associated color temperatures from the flux ratio of the two bands⁵ are shown in Figure 1. Assuming a standard color between V and the IRAC

⁵ Following the same procedure as in Su et al. (2019), the uncertainties in the color temperatures of the excesses includes 1.5% of the stellar output. Because the IRAC photometry include both binary components, the representative errors are overestimated.

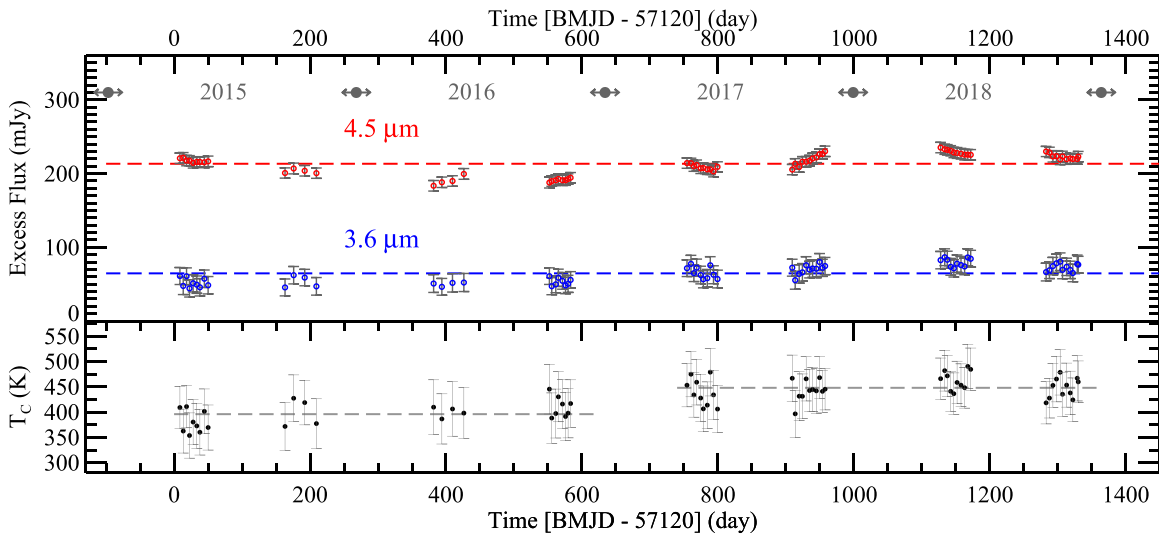


Figure 1. Time-series Spitzer observation for the HD 113766 system where the upper panel shows the excess disk emission at 3.6 and 4.5 μm and the lower panel shows the derived color temperature. In the upper panel, the colored horizontal lines represent the average disk values over the four years of Spitzer data. In the lower panel, the average color temperatures (396 ± 24 K and 448 ± 23 K), using the segments of two-year Spitzer data, are shown as the two horizontal dashed lines. There is a 2σ difference in the long-term observed color temperature (for details see Section 2.1).

bands, the two binary components should be of equal brightness for those bands. As a result, correcting for the assumed nonvariable emission of component B, the intrinsic variability is about twice that observed, i.e., $\sim 10\%$ – 15% (peak-to-peak).

The four years of warm Spitzer data show that the dust emission in the HD 113766 system exhibits nonperiodic variability at both 3.6 and 4.5 μm with peak-to-peak changes at 10%–15% levels (relative to the flux from component A). There is no strong trend in the overall flux evolution, except that the data taken in the first (last) two years are systematically lower (higher) than the four-year average values ($F_{\text{IRE},3.6} = 64.7$ mJy and $F_{\text{IRE},4.6} = 213.3$ mJy) as shown in the upper panel of Figure 1. This weak trend is also seen in the color temperature: an average of 396 ± 24 K is derived using the data in the first two years, compared with an average of 448 ± 23 K in the last two years. There is a 2σ positive correlation between the long-term disk flux and color temperature. This suggests that the disk flux variation might be due to changes in dust temperature (i.e., location) if the dust emission is optically thin.

2.2. SOFIA/FORCAST

SOFIA/Faint Object infraRed CAmera for the SOFIA Telescope (FORCAST; Herter et al. 2012) observations of HD 172555 were carried out in SOFIA Cycle 4 (Program 04_0015, PI: Su) on 2016 July 20. Data were obtained in (1) the grism mode using G111 (covering 8.4–13.7 μm with a resolution of $R = 130$ – 260) and G227 (17.6–27.7 μm , $R = 110$ – 120), both using the 4"7 slit; and (2) the imaging mode with the F111 ($\lambda_{\text{eff}} = 11.1$ μm , $\Delta\lambda = 0.95$ μm) and F242 ($\lambda_{\text{eff}} = 24.2$ μm , $\Delta\lambda = 2.9$ μm) filters in the two-point chopping configuration and a chop throw of 45". Observations for HD 113766 were carried out in SOFIA Cycle 5 (Program 05_0019, PI: Su) on 2017 August 3 using similar instrumental settings. Details about the observations are given in Table C1.

All SOFIA data were processed by the SOFIA Science Center with the pipeline “FORCAST_REDUX” ver. 1_2_0 for basic reduction. We used the pipeline-produced science-ready, Level-3 data for further analysis. For imaging data, the Level-3

Table 1
FORCAST Imaging and Spectroscopic Photometry^a

| HD | F111 | F242 | G111 | G227 |
|--------|-----------------|-----------------|-----------------|-----------------|
| 172555 | 1.45 ± 0.13 | 0.62 ± 0.37 | 1.35 ± 0.24 | 1.00 ± 0.29 |
| 113766 | 2.44 ± 0.17 | 1.10 ± 0.21 | 2.53 ± 0.20 | 1.51 ± 0.33 |

Notes.

^a All fluxes are given in units of Jansky.

products are not subtracted, merged, and flux calibrated; for spectroscopic data, the Level-3 products also include the optimally extracted, coadded 1D spectrum (see FORCAST Data Handbook, <https://www.sofia.usra.edu/>).

Both sources should be pointlike in the SOFIA measurements. Aperture photometry was performed for the imaging data. The centroid of the source was first determined by fitting a 2D Gaussian function, and then used to center the aperture. The nominal aperture photometry setting for bright calibrators is an aperture with a radius of 12 pixels (~ 4 times the beam defined as the FWHM), with a sky annulus of 15–25 pixels. However, our sources are much fainter than the bright calibrators (i.e., the photometric noise is dominated by the background), so a smaller aperture setting with an aperture correction is more suitable. For each of the Level-3 image products, we measured the photometry using an aperture setting of 6 pixels and a sky annulus between 6 and 10 pixels. We determined the aperture correction using multiple data sets for four bright flux calibrators observed in the F111 and F242 filters (see Appendix C). The aperture correction factors are 1.127 ($\pm 1.6\%$ uncertainty) and 1.204 ($\pm 4.8\%$ uncertainty) for the F111 and F242 filters, respectively. We estimated the photometric uncertainty as the standard deviation of measurements in seven nonoverlapping apertures in the nominal sky annulus region. For the multiple observations in the F111 filter, we determined an average, weighting by the uncertainty associated with each of the images. An additional 6% flux calibration uncertainty (FORCAST Data Handbook) was also added in quadrature. The final measured photometry is given in Table 1.

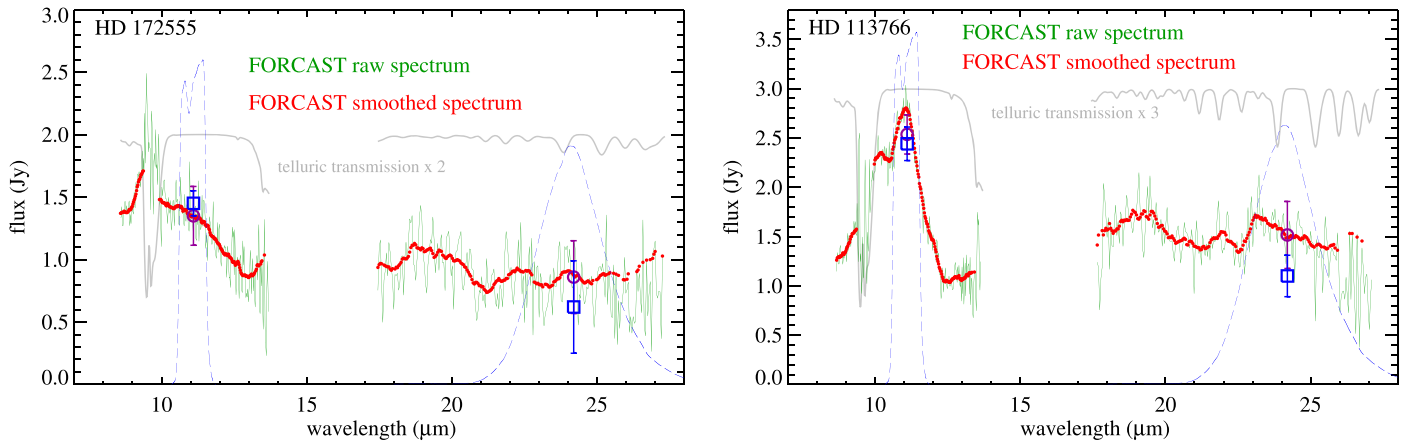


Figure 2. SOFIA spectra of the HD 172555 (left) and HD 113766 (right) systems. The FORCAST Level-3 raw spectrum is shown as the thin green line, overlaid with a smoothed one (red dots; for details see Section 2.2). The thin gray line represents the estimated telluric transmission associated with the data. The data points are discarded when the transmission is below 70% (particularly the $9.6 \mu\text{m}$ region due to the atmospheric ozone band). The purple open circles mark the synthesized flux density using the transmission curves (dashed blue lines) of the F111 and F242 filters. The photometry obtained in the F111 and F242 images was shown as blue open squares. All error bars are 1σ uncertainty.

Figure 2 shows the Level-3 spectroscopic results. The wavelength sampling in the default data output is finer than the spectral resolution of the instrument. We first smoothed the raw data (for both grisms) to a uniform resolution of $R = 80$ by including data points that have a signal-to-noise ratio (S/N) greater than 3. Although SOFIA generally flies above 99% of Earth’s atmosphere, some telluric absorption is inevitable, especially in the $9.6 \mu\text{m}$ ozone band. Because telluric calibrators were not observed at the same time when the target was observed (i.e., at similar flight latitude and airmass), accurate corrections for such absorption are not possible. We excluded the data points for further analysis where the estimated telluric transmission (see the gray curves in Figure 2) is below 70%. Another flux uncertainty in the grism spectra comes when the source is not well centered in the slit during the observation. The main purpose of the imaging data is to evaluate this uncertainty. As shown in Table C1, the imaging data were taken on the same flight as the spectroscopic data, except for HD 113766 where the F242 image was taken three days earlier than the G227 spectrum. We estimated the averaged flux density and its associated uncertainty by summing over the filter transmission curves (also shown in Figure 2). The resultant synthesized photometry using the spectra is also shown in Table 1. For imaging data, the photometry accuracy ranges from as good as $\sim 7\%$ in the F111 filter to much poorer ($\sim 20\%$ up to 50%) in the F242 filter. The spectroscopic photometric accuracy is generally in the $\sim 10\%$ – 30% range. Considering the uncertainty associated with the data, the flux calibration between the imaging and spectroscopic data agrees within $\pm 1\sigma$, so no slit-loss correction is applied to the FORCAST spectra. We further determined the repeatability of FORCAST grism spectra by assessing multiyear, archival data of bright flux calibrators. A general repeatability of 6% and 10% was estimated for the G111 and G227 grism modes (for details, see Appendix C). In summary, the absolute flux uncertainty associated with the FORCAST grism spectra is in the 6%–10% range.

2.3. Spitzer/MIPS Photometry and SED-mode Data

During the Spitzer cryogenic mission, multiple observations were obtained with the Multiband Imaging Photometer for Spitzer (MIPS) instrument for both systems. For HD 172555, there are three data sets available: two of them were in photometry mode

with the 24 and $70 \mu\text{m}$ channels, and one in the MIPS-SED mode. The first set of photometry was taken on 2004 April 6 (AOR Key 3723776, PID 10) and the data were published in Chen et al. (2006); the second set was taken on 2008 May 18 (AOR Key 25964288, PID 50316). The MIPS-SED mode data were taken in 2007 October 27 (AOR Key 21942528, PID 40679). For HD 113766, two sets of MIPS data were obtained. The MIPS photometry (AOR Key 4789760, PID 84) was taken on 2004 February 23 and published in Chen et al. (2006). The other set was taken in the MIPS-SED mode (AOR Key 13625856, PID 241) on 2005 August 2.

For consistency, we re-reduced all the photometry using an in-house MIPS data pipeline. The images of the sources are pointlike in both bands; therefore, we extracted the final values using PSF fitting (for details, see Sierchio et al. 2014). For HD 172555, the MIPS photometry in 2004 is $F_{24} = 865.9 \pm 0.15 \text{ mJy}$ and $F_{70} = 226.4 \pm 5.9 \text{ mJy}$ for 24 and $70 \mu\text{m}$, respectively. The MIPS photometry in 2008 is $F_{24} = 865.9 \pm 0.15 \text{ mJy}$ and $F_{70} = 226.9 \pm 3.3 \text{ mJy}$ for 24 and $70 \mu\text{m}$, respectively. Herschel/Photodetector Array Camera and Spectrometer (PACS) photometry was also obtained at $70 \mu\text{m}$ in 2010 (see Section 2.6 and Table 2), with the result of $217.30 \pm 7.27 \text{ mJy}$. That is, there is no flux variation among 2004, 2008, and 2010 within the instrumental calibration levels (1% and 5% at 24 and $70 \mu\text{m}$, respectively). For HD 113766 (for both A and B components), the MIPS photometry from 2004 is $F_{24} = 1459.0 \pm 14.6 \text{ mJy}$ and $F_{70} = 388.2 \pm 22.4 \text{ mJy}$, which are consistent with the values reported by Chen et al. (2011). The Herschel/PACS $70 \mu\text{m}$ measurement (Table 2) from 2011 is $414.78 \pm 7.62 \text{ mJy}$, again consistent within the expected errors.

The MIPS-SED mode provides a low-resolution ($R = 15$ – 25) spectrum from 55 to $95 \mu\text{m}$, which overlaps with the MIPS $70 \mu\text{m}$ channel and provides additional spectral slope information on the disk SEDs. We extracted the raw MIPS-SED mode data from the Spitzer archive and reduced them with the MIPS instrument team in-house pipeline (for details see Su et al. 2015). Synthesized photometry for the MIPS $70 \mu\text{m}$ channel was also computed using these MIPS-SED mode spectra. For HD 172555, the 2007 synthesized photometry is $252 \pm 25 \text{ mJy}$, consistent with the MIPS $70 \mu\text{m}$ photometry obtained in both 2004 and 2008. For HD 113766, the 2005 MIPS-SED synthesized photometry is $371 \pm 37 \text{ mJy}$, consistent with the MIPS $70 \mu\text{m}$ photometry taken

Table 2
SED Measurements

| λ_{eff} (μm) | F_{tot} (mJy) | F_{IRE} (mJy) | Note | F_{tot} (mJy) | F_{IRE} (mJy) | Note |
|---|---------------------------------|---------------------------|---------------------|---------------------------|----------------------------------|---------------------|
| <u>HD 172555</u> | | | | <u>HD 113766</u> | | |
| 8.23 | 1450.97 \pm 17.20 | 327.14 \pm 22.48 | Akari, 2006 | 1308.00 \pm 65.00 | 1164.42 \pm 65.06 | Akari, 2006 |
| 11.56 | 1124.87 \pm 15.43 | 545.15 \pm 19.30 | WISE, 2010 | 1260.96 \pm 11.56 | 1187.18 \pm 11.65 | WISE, 2010 |
| 12.00 | 1520.00 \pm 60.80 | 981.18 \pm 61.75 | IRAS, 1983 | 1580.00 \pm 94.80 | 1511.45 \pm 94.81 | IRAS, 1983 |
| 17.61 | 921.00 \pm 19.60 | 667.14 \pm 5.08 | Akari, 2006 | 1428.00 \pm 50.00 | 1395.82 \pm 50.00 | Akari, 2006 |
| 22.09 | 955.79 \pm 19.17 | 793.56 \pm 19.44 | WISE, 2010 | 1665.57 \pm 18.31 | 1645.05 \pm 18.31 | WISE, 2010 |
| 23.67 | 865.90 \pm 8.66 ^a | 724.62 \pm 9.11 | Spitzer, 2004–2008 | 1459.00 \pm 14.59 | 1441.14 \pm 14.60 ^a | Spitzer, 2004 |
| 25.00 | 1090.00 \pm 54.50 | 963.25 \pm 54.56 | IRAS, 1983 | 1800.00 \pm 90.00 | 1783.99 \pm 90.00 | IRAS, 1983 |
| 60.00 | 306.00 \pm 45.90 | 284.01 \pm 45.90 | IRAS, 1983 | 622.00 \pm 62.20 | 619.24 \pm 62.20 | IRAS, 1983 |
| 70.00 | 217.30 \pm 7.27 | 201.19 \pm 7.28 | Herschel, 2010 | 414.80 \pm 7.62 | 412.78 \pm 7.62 | Herschel, 2011 |
| 71.42 | 226.78 \pm 11.34 ^a | 211.31 \pm 11.35 | Spitzer, 2004–2008 | 388.20 \pm 22.40 | 386.26 \pm 22.40 ^a | Spitzer, 2004–2008 |
| 100.00 | 103.00 \pm 7.93 | 95.16 \pm 7.93 | Herschel, 2011 | 222.50 \pm 7.55 | 221.52 \pm 7.55 | Herschel, 2012 |
| 160.00 | 59.21 \pm 19.69 | 56.19 \pm 19.69 | Herschel, 2010–2011 | 96.13 \pm 10.78 | 95.75 \pm 10.78 | Herschel, 2011–2012 |
| 1300.00 | 0.11 \pm 0.03 | 0.07 \pm 0.03 | ALMA, 2012 | 0.62 \pm 0.08 | 0.61 \pm 0.08 | ALMA, 2014 |

Notes. Photometry is given as the total (star + disk) flux (F_{tot}) and the excess flux (F_{IRE}) after photospheric subtraction. The note column gives the source of photometry and the rough date that it was taken.

^a The MIPS photometry uncertainty is limited by the calibration (1% and 5% at 24 and 70 μm , respectively); the reported uncertainty includes the calibration error added in quadrature.

in 2004. In summary, there is no flux variation (within 1% and 5% of the measurements) using the MIPS instruments. These data will be discussed together in Section 3.1.

2.4. Spitzer/IRS

Both systems have Spitzer Infrared Spectrograph (IRS) observations. For the HD 113766 system, the measurements were published by Chen et al. (2006) and Lisse et al. (2008) along with detailed mineralogical models. We simply used the published spectrum for later analysis. For the HD 172555 system, there were two sets of IRS observations. The first one was taken on 2004 March 22 using the IRS Mapping mode (AOR Key 3563264, PID 2) with a combination of low- and high-resolution modules. This data set has been published by Chen et al. (2006) and Lisse et al. (2009). The second set was taken in 2007 November 6 using IRS Staring mode (AOR Key 24368384, PID 1446) only in the second-order, low-resolution module (LL2). We extracted this LL2 spectrum from the CASSIS project (Lebouteiller et al. 2011) using the optimal extraction. The two spectra (published and unpublished LL2) are shown in Figure 3. It appears that there is a flux jump between the low- and high-resolution part of the 2004 spectrum, while the 2007 LL2 spectrum joins more smoothly with the 2004 SL data. Given that there is no flux variation in the MIPS photometry within 1% at 24 μm (Section 2.3), the flux discrepancy between the IRS spectra taken in 2004 and 2007 is most likely due to calibration issues between different modes. We scaled the 2004 high-resolution-mode data to match the 2007 LL2 data (SH module multiplied by 1.04 and LH module multiplied by 0.91), joining them smoothly with the 2004 SL data. We further smoothed the rescaled 2004 high-resolution spectrum to $R = 60$ to match the low-resolution mode; the final 2004 rescaled, smoothed spectrum is also shown in Figure 3.

Because the IRS spectrum covers the entire band of the MIPS 24 μm channel, we further compute the synthesized MIPS 24 photometry using the published and rescaled 2004 spectra. The derived MIPS 24 μm photometry is 0.969 and 0.878 Jy, before and after rescaling, respectively. The rescaled synthesized photometry is within 1.4% of the MIPS 24 μm photometry, consistent within a few percent as expected for the

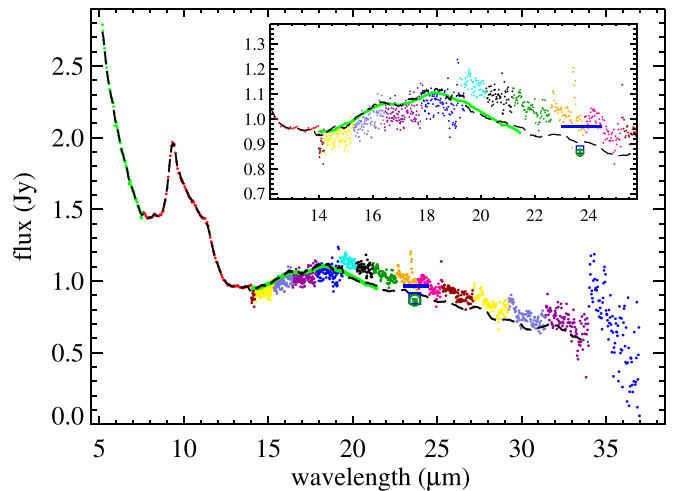


Figure 3. Spitzer IRS spectrum of the HD 172555 system. The published 2004 IRS spectrum is shown as small dots with different colors representing different orders. The 2007 LL2 spectrum is shown as a thick green line (covering 14–21.5 μm). The 2004 high-resolution-mode data were scaled to match the 2007 LL2 data and joined smoothly with the 2004 low-resolution data. A smoothed version of the 2004 spectrum is shown as the dashed black line. For comparison, the synthesized MIPS 24 photometry is 0.969 Jy (thick blue bar) before scaling, but 0.878 Jy (blue open square) after scaling. The average MIPS 24 μm photometry, 0.866 \pm 0.009 Jy is shown as a dark green open circle for comparison.

absolute flux calibration established across all Spitzer instruments (Rieke et al. 2008; Bohlin et al. 2011). A similar comparison is done for the HD 113766 system using the IRS spectrum taken in 2004 March. The IRS synthesized MIPS 24 μm photometry is 1464 mJy, matching well with the MIPS 24 μm photometry ($F_{24} = 1459.0 \pm 14.6$ mJy).

2.5. Subaru/COMICS

COMICS is the Cooled Mid-Infrared Camera and Spectrometer mounted on the Subaru 8.2 m telescope at Maunakea (Katata et al. 2000; Okamoto et al. 2003). We obtained

COMICS observations of HD 113766 on 2017 January 15. To complement these data and further search for changes in the solid-state features, we also retrieved archival COMICS data of HD 113766, taken on 2006 January 13, from SMOKA (Baba et al. 2002). Observations were taken in low-resolution, N -band spectroscopic mode with a slit width of $0''.4$ ($R \sim 170$) and a chop throw of $10''$ in 2017, and with a slit width of $0''.33$ ($R \sim 250$) and a chop throw of $12''$ in 2006. All data were taken in various short integration times on multiple (2–30) chop pairs depending on the desired S/N.

Data reduction follows standard high thermal background techniques and is executed through in-house IDL routines. First, each chop pair was differenced and examined for quality. We discarded the chop pairs showing strong residual structures due to either rapidly varying background conditions or the source not reasonably centered on the slit. The chop pairs were then rectified along the spatial axis such that the night-sky emission lines run vertically in the array coordinate. A second pass of background removal was done by subtracting the median value of background-only pixels along the spatial axis at each dispersion pixel location. Fully processed chop pairs were then median-combined, and the positive and negative spectral beams were extracted via a straight aperture sum. Uncertainties on spectral samples were calculated by determining the rms of background-only pixels and summing that in quadrature for the number of pixels in the aperture and the Poisson noise on the total summed flux in the aperture.

HD 102964 (K3III) and HR 5029 (K1III) were used as calibrators in 2006 and 2017, respectively. Assuming the calibrators are Rayleigh–Jean-like in 8–13 μm , telluric correction was performed by dividing each science spectrum by a calibrator spectrum shifted in wavelength to provide the best cancellation of the strong $\sim 9.6 \mu\text{m}$ ozone feature. The wavelength calibration was determined using a low-order polynomial fit to the position of known bright-sky emission lines. Individual calibrated science target spectra were then scaled and combined via weighted mean. Flux calibration was performed using the photometry measured from the images of the target and calibrators. We adopted the WISE W3 measurements for the calibrators and scaled them to the wavelength of the N band, at which the images were taken. For the 2006 data, both target and calibrator had imaging-only observations. For the 2017 data, no separate imaging-only observation was taken, so we had to rely on the target spectral acquisition images where the star was well displaced from the slit. The overall flux calibration is accurate at the $\sim 10\%$ level.

Final spectra showing the 10 μm range covered by COMICS are shown in Figure 4. For easy comparison, the calibrated spectra were both smoothed to $R = 100$ after rejecting points with an S/N less than 12. The shape of the 10 μm feature is very similar between the two spectra taken 11 yr apart. The overall flux also agrees well after shifting the 2006 spectrum down by 5% (within the 10% flux uncertainty). Furthermore, no significant difference is found between both the COMICS spectra and 2004 Spitzer IRS spectrum (shown as the dashed green line in Figure 4).

2.6. Other Ancillary Data

In addition to the data described in the previous subsections, we also collect all available infrared and millimeter photometry for both systems. Although both systems are saturated in the two shortest WISE bands (W1 and W2), the data from the two longer bands (W3 and W4) are not affected. We adopt the

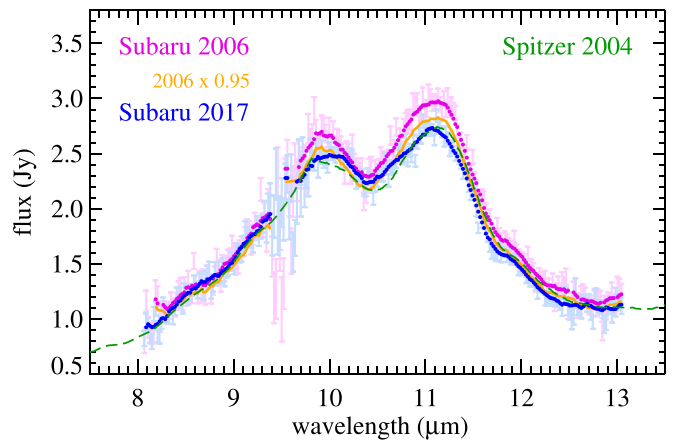


Figure 4. Subaru/COMICS spectra of HD 113766 taken in 2006 (pink color) and 2017 (blue color). The error bars show 1σ uncertainties, excluding the 10% flux calibration error. Dots represent the smoothed spectra in comparison to the 2004 Spitzer spectrum (dashed green line). The two COMICS spectra are very similar in shape and in overall flux (orange line is the 2006 spectrum shifted down by 5%).

measurements given in the ALLWISE catalog (Cutri 2014). We also include Akari/Infrared Camera (IRC) and IRAS measurements.⁶ For IRAS, we adopt the measurements from the Faint Source Catalog (FSC). Herschel/PACS observations have been reported in the literature for both systems (Olofsson et al. 2013; Riviere-Marichalar et al. 2014), but those measurements were based on an early reduction pipeline and calibration. Because both sources are not resolved by Herschel, we adopt the values from the Herschel Point Source catalog (Marton et al. 2017) where all available data were combined and processed with the final data calibration and pipeline. Table 2 lists all the valid observations along with the years they were obtained. For the measurement uncertainty, we used both the quoted statistical error and the rms of the blank sky region added in quadrature. Finally, both systems have Atacama Large Millimeter/submillimeter Array (ALMA) Band 6 (1.3 mm) observations (Lieman-Sifry et al. 2016 for HD 113766, and L. Matrà et al. 2020, in preparation for HD 172555). We further discuss the millimeter observations in Section 3.1. The collected measurements are listed in Table 2 along with the excess emission at those wavelengths after subtracting the stellar component. The disk SEDs (i.e., excess emission) are shown in Figure 5.

2.7. Variability in Mid-infrared Spectroscopy

Because Spitzer IRS spectra cover several mid-infrared bands in various infrared space missions, one can, in principle, use synthesized photometry to search for variability (similar to the comparison between MIPS 24 μm photometry and IRS synthesized photometry presented in Section 2.4). However, given the different strategies in absolute flux calibration, it is not straightforward to compare photometry directly in high fidelity.

Here we complete the search for variations by focusing on the mid-infrared spectroscopy. For the HD 113766 system, as has been discussed by Olofsson et al. (2013), the shape of the 10 μm feature remains similar when comparing the mid-

⁶ These sources are detected by neither Akari/FIS nor IRAS 100 μm .

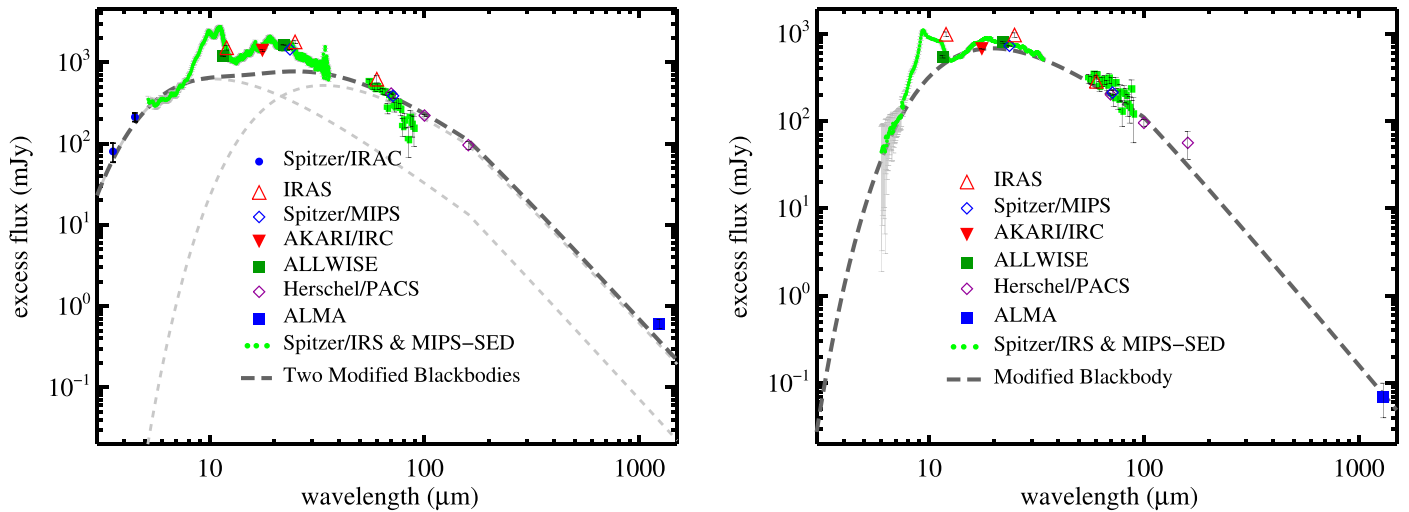


Figure 5. Spectral energy distribution of the debris emission in the HD 113766 (left) and HD 172555 (right) systems. Observed data are shown as various color symbols given on the plot. The associated error bars are the 1σ uncertainty, except for the IRAC measurements for HD 113766A where the error bars reflect the range of variations. For the HD 113766 system, the disk continuum (dark gray, long-dashed line) can be described as the the sum of two modified blackbody functions (light gray, dashed lines) for the inner and outer parts, while only a single such function is needed for the HD 172555 system.

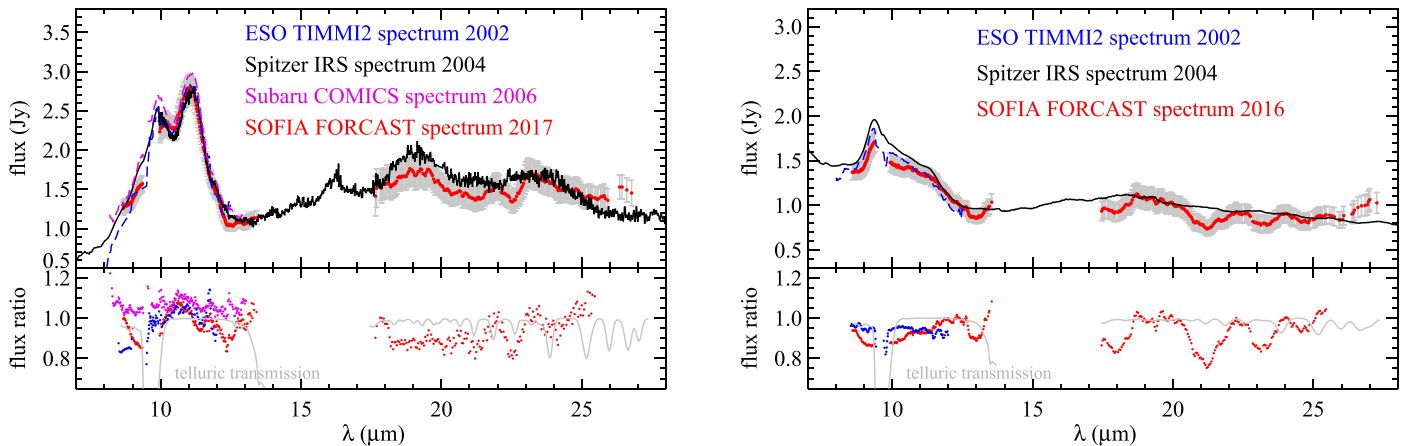


Figure 6. Comparison of mid-infrared spectra obtained over ~ 15 yr span: left for the HD 113766 system and right for the HD 172555 system. The upper panel of the plots shows the spectra in flux level, while the lower panel shows the flux ratio relative to the Spitzer spectrum taken in 2004. The gray bars show the 1σ uncertainty for the SOFIA spectrum (6% for G111 and 10% for G227). In the $10\ \mu\text{m}$ region covering the prominent solid-state features from submicron grains, no significant (more than 20%) change is found. Variation at the $\lesssim 10\%$ level might be present, but cannot be confirmed due to uncertainties across different telescopes/instruments.

infrared spectra obtained by the Very Large Telescope (VLT)/VLT Imager and Spectrometer for mid-Infrared in 2009 and 2012 to the 2004 Spitzer spectrum; however, the overall level is hard to quantify due to the difficulty in correcting for atmospheric absorption. Figure 6(a) shows the comparison of the spectra taken with TIMM12 at ESO in 2002 (Schütz et al. 2005), Spitzer in 2004, Subaru in 2006, and SOFIA in 2017. Overall, the shape of the $10\ \mu\text{m}$ feature is very similar with a subtle (up to 15%, $\sim 2\sigma$) difference in the both the blue and red sides of the feature for all four spectra. In the $20\ \mu\text{m}$ region, the overall flux level in the 2017 SOFIA spectrum is consistently lower than the 2004 Spitzer spectrum by $\sim 10\%$ (see the flux ratio in the bottom panel), but still within 1σ . Some of the large difference in flux occurs at the wavelengths where the atmospheric transmission is the worst. We do note that the blue and red sides of the $10\ \mu\text{m}$ feature cover the wavelength region where the features of submicron-size silica grains are present (Koike et al. 2013), and the nominal atmospheric transmission in this region is above 90%. The subtle difference in the $10\ \mu\text{m}$ shape might be due to a change in the amount of

silica grains, but this cannot be confirmed because of the calibration uncertainty.

We observe a similar behavior for the mid-infrared spectra in the HD 172555 system (Figure 6(b)). No change in the $20\ \mu\text{m}$ region within 10% is detected between Spitzer 2004 and SOFIA 2016 spectra, and the shape of the $10\ \mu\text{m}$ region shows a subtle change near the wavelength region at which the silica features are present; however, the tentative change (less than 3σ) cannot be confirmed. In summary, no change (more than 20%) is detected in the mid-infrared spectra over a ~ 15 yr span for both systems. Variations of $\lesssim 10\%$ might be present (particularly in the region of silica features); however, they cannot be confirmed due to calibration uncertainties across telescopes/instruments.

3. Discussion

3.1. Disk Structures Inferred from SED Models and Spatially Resolved Images

There are various SED models for both systems in the literature. Depending on whether the fits include prominent

solid-state features and/or excess emission longward of $100\ \mu\text{m}$, the derived dust temperatures and the number of components in the models vary from study to study. For example, excluding the infrared bands that cover the dust features ($\sim 8\text{--}25\ \mu\text{m}$), we determine that the disk emission in HD 172555 requires only one modified blackbody ($T_d \sim 250\ \text{K}$) to fit the disk SED, while the one in HD 113766 requires two ($T_d \sim 490\ \text{K}$ and $150\ \text{K}$) such functions⁷ (Figure 5). When primarily fitting the solid-state features presented in the IRS spectra, $335\ \text{K}$ and $490\ \text{K}$ are derived for HD 172555 and HD 113766, respectively (Lisse et al. 2008, 2009). In the latter case, an additional $\sim 75\ \text{K}$ component is required to fit the $70\ \mu\text{m}$ excess, suggesting two separate components in the HD 113766 disk (Lisse et al. 2008). How to translate these dust temperatures to physical distance from the star depends significantly on the underlying grain properties, particularly the minimum grain sizes in the debris (Thebault & Kral 2019).

High-angular-resolution imaging studies have also been performed for both systems from the ground, providing direct constraints on the location of the dust emission. Smith et al. (2012) presented a comprehensive mid-infrared study of these two systems including interferometric, spectroscopic, and narrowband imaging observations obtained with the VLT. For the HD 113766 system, Olofsson et al. (2013) confirmed that the disk has two distinct components by simultaneously fitting the imaging data from the VLT and the well-sampled infrared disk SED, including the solid-state features. With the pronounced dust features and the mid-infrared interferometric measurements, the inner disk in HD 113766 is relatively constrained to radii of $0.5\text{--}1.2\ \text{au}$ (including 1σ margin) from the star. The outer disk is estimated to lie at radii of $\sim 8\text{--}16\ \text{au}$ (i.e., a diameter of $0''.5$), consistent with not being resolved in the N - and Q -band images (Smith et al. 2012). Surprisingly, the HD 113766 system is marginally resolved at $1.24\ \text{mm}$ by ALMA (Lieman-Sifry et al. 2016) with a synthesized beam of $1''.39 \times 0''.81$, suggesting the millimeter emission from the system is extended beyond $44\ \text{au}$ from the star. Because the bulk of the disk emission peaks at mid-infrared wavelengths (see left panel of Figure 5), it is difficult to reconcile the large difference in the disk sizes measured at mid-infrared and millimeter if both come from the same outer disk component. A SED model using the parameters derived by Olofsson et al. (2013) and a power-law extrapolation using the measured far-infrared fluxes both predict a total $1.24\ \text{mm}$ flux that is smaller than the ALMA value by a factor of 2. This suggests that either the ALMA detection comes from a different cold component that predominantly emits in the millimeter wavelengths or that the ALMA detection is contaminated by background galaxies.

For the HD 172555 system, mid-infrared interferometric observations completely resolve out the disk emission, suggesting that the bulk of debris emission is outside of $0.5\ \text{au}$ from the star (Smith et al. 2012). The disk was first resolved in the thermal infrared (at $\sim 20\ \mu\text{m}$, Smith et al. 2012) and later in polarized scattered light (Engler et al. 2018). Mid-infrared imaging suggests that the disk is inclined by $\sim 75^\circ$

from face on. Assuming a Gaussian-ring-like model, the bulk of disk emission at $20\ \mu\text{m}$ is peaked at $7.7 \pm 1.5\ \text{au}$ from the star (Smith et al. 2012), which is consistent with the scattered-light result ($\sim 8.5\text{--}11.3\ \text{au}$, Engler et al. 2018). Furthermore, both studies suggest that there is significant material interior to the bulk emission of the disk (less than $8\ \text{au}$). The system also has an ALMA observation at $1.3\ \text{mm}$ where both the thermal dust continuum and CO (2–1) gas emission are detected (L. Matrà 2020, private communication). The disk is not spatially resolved in the dust continuum, but spectrally resolved in the CO emission that is best described by a narrow ring peaked at $\sim 8\ \text{au}$ from the star.

In summary, the HD 113766 disk is complex and consists of an inner, $\sim 1\ \text{au}$ component that emits mainly in the Spitzer IRAC and IRS $10\text{--}20\ \mu\text{m}$ wavelengths, and an outer, $\sim 10\ \text{au}$ component that emits its bulk emission in the far-infrared and millimeter wavelengths. On the contrary, the HD 172555 disk appears to be one broad component peaked at $\sim 8\ \text{au}$ from the star with material existing interior and exterior to the peak radius. We note that the location of the pronounced solid-state features is near $\sim 6\ \text{au}$, inferred from the best-fit dust temperature (Lisse et al. 2009), apparently interior to the peak radius. However, given the degeneracy of SED modeling, the relative location of the material that produces these features is uncertain.

3.2. Implications

As has been discussed in the literature, the amount of small (submicron to micron size) grains that produce the prominent solid-state features must be stable over a decadal timescale, as reinforced by the new Subaru and SOFIA observations, so that the shape and relative strength of the $10\ \mu\text{m}$ feature (within $\sim 10\%$ level) remain the same. The relative stability implies that the dust production and loss rates are balanced. The production of small grains in typical debris systems mainly comes from the collisional cascades within the swarm of particles, while the loss mechanism is dominated by collisional destruction followed by radiation pressure blowout for stars as luminous as these two. Although the exact size of grains that are subject to radiation blowout depends sensitively on the properties of the stars (mass and luminosity) and dust grains (composition, sizes, and porosity), the blowout limit is around $\sim 1\ \mu\text{m}$ in both systems if one assumes compact, silicate-like composition (which generally gives the smallest blowout sizes). Arnold et al. (2019) concluded that the blowout size could be an order of magnitude larger when mixing different kinds of compositions and porosity. However, the compositions used in that study are materials commonly found in solar system interplanetary particles; minor minerals such as crystalline silicates (producers of sharp solid-state features in debris disks) are not included.

We first review whether the dust in these systems can be produced in typical collisional cascades. We adopted the analytical formula and criterion in Wyatt et al. (2007) for the assessment. Due to the necessary assumptions and associated uncertainties, the adopted model requires a high threshold (a factor of 1000) to differentiate systems that are most likely in a transient state from the ones that are consistent with steady-state collisional cascades. For the HD 172555 system, the following parameters were used: $1.8 M_\odot$, $9 L_\odot$, and $20\ \text{Myr}$ for the star with a planetesimal belt at $r \sim 9\ \text{au}$. The resultant maximum infrared fractional luminosity (f_{max}) is 2×10^{-4} for

⁷ The modified blackbody is a function of wavelength λ given by $B_\nu(\lambda, T_d)$ for $\lambda < \lambda_0$ and $\alpha(\lambda_0/\lambda)^\beta B_\nu(\lambda, T_d)$ for $\lambda > \lambda_0$, where B_ν is the Planck function, and the temperature T_d and scaling factor α , λ_0 , and β are free parameters. This function is widely adopted for fitting debris disk SEDs to account for the fact that the emission comes from grains in all sizes, and that grains will not act as perfect blackbodies, in particular emitting inefficiently at wavelengths longer than their own size; λ_0 and β are thus related to the grain size distribution.

a typical collisional cascade system. The observed infrared fractional luminosity is only three to four times larger than this value, i.e., within the uncertainties the dust in the HD 172555 can be produced by a massive planetesimal belt. For the HD 113766 system, $1.5 M_{\odot}$, $4 L_{\odot}$, and 20 Myr were used for the star, and planetesimal belts at $r \sim 1$ au and $r \sim 10$ au were assumed. The corresponding f_{\max} is 3×10^{-6} and 6×10^{-4} for the inner and outer planetesimal belts. The observed fractional luminosity is $\sim 3.3 \times 10^{-2}$ for the inner belt and $\sim 7 \times 10^{-4}$ for the outer one (Olofsson et al. 2013). That is, the dust in the outer belt can arise in a conventional collisional cascade, but that in the inner belt is transient (i.e., the observed amount is $\sim 10,000$ times the maximum value for a steady state).

If this fine dust is transient, one might expect significant changes in the solid-state features given the amount of submicron-size grains ($\sim 10^{23}$ g) and their short lifetimes (~ 1 yr) due to radiation blowout. However, there is no convincing case that such changes are seen. Recent studies of two extremely dusty systems, BD+20 307 (two late F-type binary; Thompson et al. 2019) and HD 145263 (F4V; Lisse et al. 2020), also suggest that there is no large-degree (more than 20%) change in the mid-infrared spectra over a decade.⁸ A common question in the literature has been: how did such tiny grains get created in the first place? The concern is that it may be difficult to create such abundant submicron-size grains in a typical, optically thin, collisional cascade debris system because of the short lifetime to radiation pressure blowout for their parent \sim micron-size grains. However, Thebault & Kral (2019) have calculated new models of collisional cascades and suggest that submicron-size grains below the blowout size can accumulate in sufficient number potentially to resolve this conundrum for bright disks around early-type stars (such as HD 172555). Their model has a number of uncertainties, such as operating only in 1D, having to make extrapolations of the strength law toward the submicron-size regime, etc. It would also make it puzzling that we do not observe such prominent solid-state features toward the majority of the bright disks around early-type stars with similar fractional excesses; HIP 73145 (an A2V star with $f_d \sim 8 \times 10^{-4}$) and HIP 77315 (an A0V star with $f_d \sim 2 \times 10^{-4}$) from Ballering et al. (2017) are two such examples. Furthermore, Thebault & Kral (2019) conclude that massive debris systems around solar-like stars are not sufficiently effective at preserving grains smaller than the blowout size to result in pronounced solid-state features in the mid-infrared. Further work is needed to test their suggestion.

Although such a steady-state solution might be attractive in nonevolving systems, it is less convincing for systems with disk variability, such as HD 113766. The recent CO gas detection (L. Matr a 2020, private communication) and the large amounts of atomic species (Kiefer et al. 2014; Riviere-Marichalar et al. 2014; Grady et al. 2018) in the HD 172555 system also argue for a transient phenomenon. In these active systems, an optically thick cloud of debris produced by a violent impact between two bodies with sizes of large asteroids or protoplanets might be a better explanation for the presence of abundant submicron grains. The presence of such optically thick debris clouds is inferred to explain the complex disk light curves observed in some extremely dusty, young debris disks (Meng et al. 2014; Su et al. 2019). Given the mass and confined

volume resulting in a large impact, the impact-produced cloud is very likely to be optically thick initially before thinning by Keplerian shear. Such an environment provides perfect conditions to generate overabundant small grains because stellar photons can only efficiently remove the small grains at the surface of the cloud. Once the impact-produced cloud becomes optically thin, the small grains that are subject to radiation pressure blowout would quickly be removed from the system, likely resulting in a rapid drop in the system’s flux due to the decrease of dust temperatures, as has been observed in the ID8 system (Su et al. 2019). However, there may be sufficient time to generate even smaller grains within the cloud that are not subject to radiation pressure blowout and are revealed only after the cloud becomes optically thin. This might be the case for the HD 172555 system where Johnson et al. (2012) suggested that tiny, $0.02 \mu\text{m}$ -size obsidian grains are not subject to radiation blowout. Similarly, $0.1 \mu\text{m}$ -size silicate grains in the HD 113766 system are expected to be stable due to the same reason. In this scenario, the prominent infrared features would remain stable for a long time. The timescale on which we could expect them to change would then be set by the (much longer) Poynting–Robertson (P–R) drag timescale of these fine grains, which is $\sim 1.3\text{--}7.7 \times 10^2$ yr for the HD 113766 inner component and $\sim 1.6\text{--}3.6 \times 10^4$ yr for the HD 172555 system.⁹

For the HD 113766 system, there appears to be a conflict between the variability from warm Spitzer observations and the stable solid-state features in the mid-infrared. We note that the level of variability observed at 3.6 and $4.5 \mu\text{m}$ is consistent with that of the possible changes in the mid-infrared spectra from Spitzer, Subaru, and SOFIA if the dust emission is optically thin. If some part of the $3.6/4.5 \mu\text{m}$ emission is optically thick, one would not expect the IRAC flux to track the optically thin solid-state features in the mid-infrared. It is also likely that the inner disk component has a background population of \gtrsim kilometer-size planetesimals, creating additional low-level variations traced by the high-precision IRAC photometry. The tentative (2σ) positive correlation between the long-term disk flux and color temperature (see Section 2.1) might be due to a change in dust location under the optically thin assumption. A 13% change in the color temperature is then translated to a 27% change in location ($T_d \sim 1/\sqrt{r}$). A dust clump/arc in a modestly eccentric ($e \sim 0.12$) orbit at 1.5 au can produce such a flux/temperature variation. However, the typical grain sizes in the clump/arc have to be very small to match the observed color temperature, consistent with the hypothesis of a stable population of submicron grains responsible for the pronounced solid-state features. Future observations in the range of $3\text{--}5 \mu\text{m}$ can further test the hypothesis of an eccentric clump/arc in the HD 113766 inner component.

3.3. Can Dust Composition Alone Tell us How Small Grains are Generated in Young Dusty Debris Systems?

The infrared wavelength range contains the fundamental bending, stretching and skeleton modes of solid-state species. Consequently, infrared spectroscopy of molecular clouds and protoplanetary disks (van Dishoeck 2004; Sargent et al. 2009)

⁸ See Appendix C for the discussion about BD+20 307.

⁹ The P–R timescale is formulated as $\tau_{\text{PR}} = cr^2/(4GM_*\beta) \sim 800 \text{ yr } (r/\text{au})^2 (M_{\odot}/M_*)(0.5/\beta)$, where c is the speed of light, G is the gravitational constant, and M_* is the stellar mass. We assume $\beta = 0.5$ to calculate the P–R timescale as a minimal value.

provides crucial information on the sizes and composition of dust grains, which are the building blocks embedded in \gtrsim kilometer-size planetesimals within a planetary system. We can learn about these building blocks through infrared spectroscopy, when they are released by planetesimals shattered to form second-generation dust debris. In addition to coagulation, dust grains in the protoplanetary disks have also been through various heating/cooling processes so that crystalline forms of silicates (such as olivine, pyroxene, and silica) are commonly found in the more evolved stages of planet-forming disks (Sargent et al. 2009), while such crystalline grains are largely absent in the interstellar medium (Kemper et al. 2004). Therefore, it should not be a surprise to find crystalline silicates in debris disks if these processed grains are stored in planetesimals. Nonetheless, Spitzer/IRS studies of debris systems reveal that the majority of these disks have a featureless dust continuum in the mid-infrared (Chen et al. 2005; Mittal et al. 2015). This is understandable given that the typical blowout size is $\sim 1 \mu\text{m}$ in these systems and that grains larger than a few microns have weak and broad features.

In contrast, conspicuous crystalline solid-state features in the mid-infrared are characteristic of extreme debris systems (Song et al. 2005; Lisse et al. 2008, 2020; Rhee et al. 2008; Weinberger et al. 2011; Fujiwara et al. 2012; Olofsson et al. 2012, 2013), produced by warm submicron-size silicates similar to the ones commonly found in Herbig Ae/Be (Bouwman et al. 2001) and T-Tauri disks (Kessler-Silacci et al. 2006; Sargent et al. 2009). Despite different modeling approaches from study to study, the strength of the features typically requires $\sim 10^{20}$ – 10^{25} g of submicron-size grains in optically thin environments. These features are similar to laboratory-measured features from meteoric, terrestrial crustal, and mantle material measured in powder form, implying that the debris dust in these young systems underwent various degrees of shock and/or high-temperature events (Morlok et al. 2014; de Vries et al. 2018). Although such connections in dust mineralogy between debris disks and highly altered/processed material have been found in the solar system, similar links seem to be present in the protoplanetary stage of evolution when gas was still present. Therefore, identifying the dust species alone does not tell us when these altered grains were formed either in the recent or far past. However, given the issues of retaining such a large amount of these submicron-size grains (as discussed in the previous section), it becomes clear that they have to be generated in the recent past.

Another indication of recent violent events in debris disks is the detection of freshly condensed submicron-size silica smokes (Rhee et al. 2008; Lisse et al. 2009; Fujiwara et al. 2012). Indeed, this is thought to be the process that formed the first submicron-size solids in the solar nebula, which is also verified by laboratory experiments (see the book by Loretta & McSween 2006). However, this kind of condensation took place in a low-pressure environment, $\sim 10^{-3}$ – 10^{-6} bar, in the early solar nebula (Ebel 2006). Such an environment is very different from the high-pressure (and temperature) condition within a vaporizing collision between two large bodies (Johnson & Melosh 2012). The sizes of the vapor condensates generated in a violent collision between two large planetesimals depend sensitively on the collisional conditions, but are nearly all larger than $10 \mu\text{m}$ for impactors larger than 10 km (Johnson & Melosh 2012). Roughly millimeter-size impact glasses (spherules and shards) are commonly found in the

sample returns from the Apollo mission (see the review by Zellner 2019). Most importantly, these impact-produced glasses will not give rise to the prominent solid-state features displayed in young dusty debris disks, unless they are broken up into much smaller grains.

Recently, extreme space weathering has been proposed to break up larger grains and to explain the “unique” dust mineralogy in the young (~ 11 Myr, Pecaut et al. 2012), dusty ($f_d \sim 1.2 \times 10^{-2}$, Mittal et al. 2015) HD 145263 system (Lisse et al. 2020). A key ingredient to the space weathering model is supermassive flares or intense X-ray/ultraviolet (UV) radiation from the young star, a condition that is applicable to the AU Mic system (MacGregor et al. 2020) and many other young late-K- and M-type stars. However, there is no detectable solid-state feature in the AU Mic system (see the IRS spectra provided by CASSIS project, <http://cassis.sirtf.com/>), and pronounced solid-state features are rarely seen in late-type disks (Lawler et al. 2009; Mittal et al. 2015). Although the energetic stellar photons might be efficiently altering the surface composition of large (a few $100 \mu\text{m}$) grains as discussed by Lisse et al. (2020), they most likely vaporize small micron-size grains as suggested by Osten et al. (2013). Therefore, this mechanism cannot explain the amount of submicron-size grains required to produce the solid-state features observed in this system.

Using the same analytical estimate discussed in the previous section for HD 145263, we found $f_{\text{max}} \sim 5.2 \times 10^{-6}$, 2.6×10^{-5} , and 6.7×10^{-5} for a planetesimal belt at $r \sim 1$, 2, and 3 au assuming the same stellar parameters as in HD 113766A and an age of 11 Myr. The dust level observed in the HD 145263 system is on the borderline¹⁰ between transient dust and collisional cascade dust produced in a massive planetesimal belt. Given the amount of submicron-size grains ($\sim 10^{25}$ g; Lisse et al. 2020) and the short lifetime of their parent micron-size grains in optically thin collisional cascades, we suggest that the fine dust in the HD 145263 system, similar to the two systems we discussed in this paper, was created by transient events. A large collision, involving large-size ($\gtrsim 100$ km) asteroids that facilitated the overproduction of submicron-size grains within an optically thick impact-produced debris clump is a better scenario to explain the distinctive solid-state features observed in these young systems.

4. Conclusion

We present multiepoch, infrared photometric and spectroscopic data for two young (~ 20 Myr), extremely dusty debris systems around HD 113766A and HD 172555. High-precision ($S/N > 100$, i.e., 1% photometric accuracy) 3.6 and $4.5 \mu\text{m}$ data were obtained during the Spitzer warm mission to assess the disk variability. We found no variability for HD 172555 within 0.5% of the average fluxes in either bands with the data taken between 2013 and 2017. These measurements are consistent with the expected photospheric values to within 1.5% (i.e., no infrared excess). For the HD 113766 system, on the contrary, nonperiodic variability was detected at ~ 10 – 15% peak-to-peak levels relative to the brightness of the primary, from 2015 to 2018. There is a 2σ positive correlation between the long-term disk flux and color temperature, suggesting that

¹⁰ We refer to it as borderline because only the smallest (1 au) planetesimal belt location meets the criterion, by more than a factor of 1000, as in a transient state, while others are only larger by a few 100.

the variation might be due to changes in dust temperature (i.e., location) if the dust emission is optically thin.

Low-resolution, mid-infrared spectra obtained with SOFIA/FORCAST and Subaru/COMICS are presented in this study. FORCAST grism spectra covering 8.4–13.7 μm (G111 mode) and 17.6–27.7 μm (G227 mode) were obtained in 2016 and 2017 for HD 172555 and HD 113766, respectively. Using similar grism data from bright flux standards available in the SOFIA archive, we further determined an overall 1σ of 6% (for G111 mode) and of 10% (for G227) uncertainties associated with these SOFIA spectra, including the flux calibration and instrumental repeatability. Additionally, COMICS 8–13 μm spectra taken in 2006 and 2017 were presented for the HD 113766 system. We find that the shape of the 10 μm feature and the overall flux level (within 10%) are very similar between the two spectra taken 11 yr apart.

We also present multiepoch Spitzer MIPS data obtained during the cryogenic mission including photometry at both 24 and 70 μm channels and MIPS-SED mode data. No flux variation (within 1% at MIPS 24 μm and 5% at MIPS 70 μm) was found for HD 172555 using data from 2004 to 2008 and HD 113766 using data from 2004 to 2005. Combined with other multiwavelength ancillary data, these data were used to discuss the disk structure in each of the systems. The HD 113766 system has a two-component disk with an inner ~ 1 au component that emits mainly in the ~ 3 –20 μm region, and an outer ~ 10 au component that dominates the far-infrared and millimeter wavelengths. The HD 172555 disk appears to have one component peaked at ~ 8 au from the star with significant amounts of material interior and exterior to the peak radius.

We assess the temporal variability using the mid-infrared spectra obtained over a ~ 15 yr span for both systems. Using the high-quality Spitzer IRS spectrum as a reference, we found no significant (more than 20%) change in either the shape of the prominent 10 μm solid-state feature or the overall mid-infrared flux levels for both systems. Variations of $\lesssim 10\%$ might be present on the blue and red sides of the 10 μm feature where the dust features from submicron-size silica are generally found. However, such subtle changes cannot be confirmed due to calibration uncertainties and need to be confirmed with future observations obtained with a more stable instrument such as the James Webb Space Telescope/Mid-Infrared Instrument.

The amount of submicron-size grains required to produce the prominent 10 μm feature is on the order of 10^{23} g for both systems (Lisse et al. 2009; Olofsson et al. 2013). Adopting the analytical calculation and criterion set by Wyatt et al. (2007), we verified that the amount of submicron-size grains in the inner component of the HD 113766 system is unlikely to be produced in a typical collisional cascade system, while its outer component and the HD 172555 disk are consistent with steady-state collisional cascades. For massive debris disks around early-type stars (such as HD 172555), new collisional cascade calculations by Thebault & Kral (2019) suggest that a sufficient amount of submicron-size grains can accumulate and produce stable and pronounced 10 μm features. Nevertheless, some other ingredients might be missing in their model because the majority of early-type massive disks show featureless dust continua in the mid-infrared.

Extreme space weathering has been proposed to explain the unusual dust mineralogy in the HD 145263 system (Lisse et al. 2020), where the host star is very similar to HD 113766A (both

early F-type and young). We do not think space weathering is a viable explanation for the presence of abundant submicron-size grains. Energetic photons from supermassive flares around young solar-like stars are most likely to destroy/vaporize small dust grains present in the disk. Although intense space weathering might be able to alter the surface composition of large grains and preserve the usual composition as they broke up in subsequent collisions, this mechanism cannot explain the fact that the majority of the debris systems around young, active stars show featureless mid-infrared spectra. We also note that submicron-size crystalline silicates and silica are commonly found in planet-forming disks when gas was still present (Bouwman et al. 2001; Kessler-Silacci et al. 2006; Sargent et al. 2009). Therefore, dust species alone do not inform us when these highly processed grains were formed. They could be formed in the early protoplanetary disk stage in which those altered grains were stored in planetesimals and subsequent collisional grinding among planetesimals released them into the circumstellar environment. They could also be formed in the recent past when amorphous fine grains experienced high-temperature events such as violent impacts involving large asteroidal or planetary bodies.

Finally, we suggest that disk variability might be a useful signpost to reveal highly altered grains generated in the recent past for young and dusty exoplanetary systems. In this case, such as the inner component of the HD 113766 system, the abundant submicron-size grains might be due to the intense collisions among their parent millimeter-size vapor condensates produced in an initially optically thick, impact-produced debris clump. Such an optically thick environment would easily lead to an overproduction of fine grains that are smaller than the typical blowout size in the center of the clump because stellar photons cannot easily penetrate. Once the impact-produced clump becomes optically thin as it is stretched by Keplerian shear, the grains subject to radiation pressure blowout (just slightly smaller than the blowout size) are quickly removed from the system, likely resulting in a rapid flux drop in the system’s infrared output (a phenomenon that has been seen in the ID8 system; Su et al. 2019). If the impact-produced cloud has enough time in the optically thick condition to allow for the production of even smaller grains that are not subject to radiation blowout (~ 0.02 μm glassy silica in HD 172555 and ~ 0.1 μm crystalline silicates in HD 113766A), these fine grains would be stable after the clump/arc becomes optically thin as suggested by Johnson et al. (2012). If there is no additional input for the submicron-size grains such as additional large impacts, the lifetime of these features should be unchanged within the P–R timescale, i.e., beyond the human lifetime for these two systems. Nevertheless, for the systems with such features located on less than a 0.2 au around 1–2 M_{\odot} stars, changes within a couple of decades are possible. For the HD 113766 system, the long-term flux trend and the positive correlation between disk flux and color temperature observed by Spitzer are consistent with the presence of such an optically thin clump/arc on a modestly eccentric orbit in the inner component. The lifetime of such an impact-produced clump/arc depends sensitively on the impact condition and subsequent collisional evolution, and the asymmetric phase can last for a few hundred orbital evolutions (Jackson et al. 2014; Kral et al. 2015).

This work is based on observations made with the Spitzer Space Telescope, which is operated by the Jet Propulsion Laboratory, California Institute of Technology, and made with the NASA/DLR Stratospheric Observatory for Infrared Astronomy (SOFIA). SOFIA is jointly operated by the Universities Space Research Association, Inc. (USRA), under NASA contract NAS2-97001, and the Deutsches SOFIA Institut (DSI) under DLR contract 50 OK 0901 to the University of Stuttgart. This work has made use of data from the European Space Agency (ESA) mission Gaia (<https://www.cosmos.esa.int/gaia>), processed by the Gaia Data Processing and Analysis Consortium (DPAC, <https://www.cosmos.esa.int/web/gaia/dpac/consortium>). Funding for the DPAC has been provided by national institutions, in particular the institutions participating in the Gaia Multilateral Agreement. Financial support for this work was provided by NASA through award # SOF04-0015 and SOF05-0019 issued by USRA, and the ADAP program (grant No. NNX17AF03G). C.M. acknowledges support from NASA through grant 13-ADAP13-0178. Based in part on data collected at Subaru Telescope and obtained from the SMOKA, which is operated by the Astronomy Data Center, National Astronomical

Observatory of Japan. We thank the anonymous referee for a thorough reading and prompt report. K.Y.L.S. thanks C. Chen for providing published IRS spectra used in this work.

Facilities: Spitzer (IRAC, IRS, MIPS), SOFIA (FORCAST), Subaru (COMICS).

Appendix A Warm IRAC Photometry for HD 113766 and HD 172555 Photometry

The measured fluxes using the Spitzer IRAC observations described in Section 2.1 are given in Tables A1 and A2 for the HD 113766 and HD 172555 systems, respectively. For HD 113766, the quoted fluxes are for both the A and B components. As discussed in Section 2.1, only the A component has an infrared excess indicative of circumstellar dust. We predicted the combined stellar output from both components in Appendix B and used it to derive the excess fluxes of HD 113766A at both 3.6 and 4.5 μm (also given in Table A1). The uncertainty associated with the excess fluxes include 1.5% of the combined stellar output.

Table A1
The IRAC Fluxes of the HD 113766 System

| AOR Key | BMJD _{3.6} (day) | $F_{3.6}$ (mJy) | $E_{3.6}$ (mJy) | $exeF_{3.6}$ (mJy) | $exeE_{3.6}$ (mJy) | BMJD _{4.5} (day) | $F_{4.5}$ (mJy) | $eF_{4.5}$ (mJy) | $exeF_{4.5}$ (mJy) | $exeE_{4.5}$ (mJy) |
|----------|------------------------------|--------------------|--------------------|-----------------------|-----------------------|------------------------------|--------------------|---------------------|-----------------------|-----------------------|
| 53463040 | 57128.539790 | 788.99 | 3.67 | 61.09 | 11.52 | 57128.538250 | 676.37 | 1.80 | 220.82 | 7.07 |
| 53462784 | 57133.418070 | 775.56 | 4.26 | 47.66 | 11.72 | 57133.416540 | 676.96 | 1.96 | 221.41 | 7.11 |
| 53462528 | 57138.283870 | 788.66 | 3.29 | 60.76 | 11.40 | 57138.282350 | 673.29 | 2.00 | 217.74 | 7.12 |
| 53462016 | 57142.636470 | 772.22 | 4.17 | 44.32 | 11.69 | 57142.634950 | 673.03 | 1.41 | 217.49 | 6.98 |
| 53461504 | 57147.970320 | 779.14 | 4.33 | 51.24 | 11.74 | 57147.968810 | 670.18 | 1.89 | 214.63 | 7.09 |
| 53460992 | 57153.371310 | 777.25 | 4.44 | 49.35 | 11.79 | 57153.369770 | 671.43 | 1.60 | 215.88 | 7.02 |

Note. F and E are the flux and uncertainty including the star, while $exeF$ and $exeE$ are the excess quantities excluding the star.

(This table is available in its entirety in machine-readable form.)

Table A2
The IRAC Fluxes of the HD 172555 System

| AOR Key | BMJD _{3.6} (day) | $F_{3.6}$ (mJy) | $E_{3.6}$ (mJy) | BMJD _{4.5} (day) | $F_{4.5}$ (mJy) | $eF_{4.5}$ (mJy) |
|----------|------------------------------|--------------------|--------------------|------------------------------|--------------------|---------------------|
| 48318464 | 56455.24044 | 5316.18 | 0.85 | ... | ... | ... |
| 58766592 | 57561.96057 | 5358.98 | 1.35 | 57561.96115 | 3501.75 | 1.03 |
| 58766336 | 57571.61957 | 5352.53 | 0.75 | 57571.62014 | 3495.64 | 1.30 |
| 58766080 | 57581.74171 | 5366.15 | 1.51 | 57581.74228 | 3504.02 | 1.19 |
| 58765824 | 57591.92158 | 5337.11 | 0.85 | 57591.92215 | 3497.69 | 0.87 |
| 58765568 | 57601.00141 | 5335.97 | 0.79 | 57601.00198 | 3491.22 | 1.15 |
| 58765312 | 57716.17711 | 5325.11 | 1.22 | 57716.17770 | 3484.07 | 1.03 |
| 58765056 | 57725.60858 | 5334.20 | 0.74 | 57725.60915 | 3493.79 | 1.48 |
| 58764800 | 57736.09562 | 5384.17 | 1.45 | 57736.09620 | 3486.51 | 1.28 |
| 58764544 | 57747.12971 | 5326.71 | 0.65 | 57747.13028 | 3498.77 | 0.94 |
| 58764288 | 57755.27977 | 5337.39 | 1.00 | 57755.28034 | 3510.49 | 1.08 |

Note. The average flux densities are 5340 ± 20 mJy and 3496 ± 8 mJy at the 3.6 and 4.5 μm bands, respectively.

Appendix B Stellar Properties for the HD 113766 System

We used the photometry that contains both stars (Johnson UVB and Two Micron All Sky Survey JHK) to estimate the combined stellar output in the IRAC wavelengths. A Kurucz model with a temperature of 6750 K provides a good fit to the combined photometry and results in a total luminosity of $9.4 L_{\odot}$ at a distance of 111 pc (Gaia Collaboration et al. 2016, 2018). The derived combined luminosity is within $\sim 10\%$ of the combined value derived by Pecaut et al. (2012) after correcting for the adopted distance. The expected photospheric flux is 728 mJy at the IRAC 3.6 μm band and 456 at the IRAC 4.5 μm band.

Appendix C Details about the SOFIA/FORCAST Observations and Associated Uncertainty

As described in Section 2.2, we used the Level-3 data products provided by the SOFIA Science Center for further analysis. Table C1 gives the details about the SOFIA/FORCAST observations presented in this work, including the time of the observation, flight altitude, instrumental grism/filter, and total integration time. To assess the flux calibration and repeatability in the FORCAST data, we also made use of multiyear, archival data for bright calibrators: α Tau, α Boo, β And, and σ Lib. We used the imaging data to determine the appropriate aperture correction factor. A total of 206 “calibrated” Level-3 images was used for the F111 filter with data taken from 2013 to 2019, and a total of 22 images taken in 2016–2019 was used for the F242 filter. The aperture correction factor for a specific setting in the aperture was determined by referencing the total flux derived using the nominal aperture setting [12, 15, 25] (i.e., a radius of 12 pixels

and sky annulus of 15–25 pixels). For an aperture setting of [8, 8, 12], the aperture correction factor is 1.073 ± 0.010 for the F111 filter and 1.121 ± 0.042 for the F242 filter. For an aperture setting of [6,6,10], the factors are 1.127 ± 0.018 and 1.204 ± 0.058 for the F111 and F242 filters, respectively. Using the nominal aperture, we also confirmed the 6% flux calibration in the photometry using these bright calibrators.

For the grism data, only α Tau has more than a dozen G111 Level-3 (“combspec”) data points taken in 2016–2018, σ Lib has a handful of G227 data taken in 2014–2015, and the other two stars have a few spectra available in the archive. Note that these calibration data were taken at different flights, altitudes, and slit widths (2"4 and 4"7); so, the comparison among them reflects the overall repeatability in the long-term (multiyear) flux calibration, which is essential in assessing source variability using the grism data. For a target with spectra taken in the same flight but with two slit widths, the spectra agree within a few percent. For the G111 mode, an average of 4% repeatability is derived, but could be up to 10% level in the ozone band. For the G227 mode, an average of 10% repeatability is derived, but could be up to 20%. Including the 6% flux calibration error derived from photometry, the grism spectra have a long-term repeatability of 6% and 10% for the G111 and G227 modes, respectively. In summary, flux variation at the levels of 6% and 10% (1σ) for the G111 and G227 grism spectra is not significant. Recently, a flux increase ($\sim 10\% \pm 2\%$) in the BD+20 307 system was reported by Thompson et al. (2019) using the 2006 Spitzer and 2015 SOFIA spectrum (G111 mode). Taking the uncertainties in absolute flux calibration, stability of the instruments, and slit-loss and aperture corrections, the reported uncertainty is slightly underestimated, suggesting the tentative flux increase is at $\sim 2\sigma$ levels.

Table C1
SOFIA Observations

| Level-3 # | Filter/Grism | Date | UT | Altitude (ft) | Integration (s) |
|-------------------|--------------|-------------|------------|---------------|-----------------|
| <u>HD 172555</u> | | | | | |
| 0191 | F111 | 2016 Jul 20 | 14:38:40.3 | 43019–43020 | 26.7 |
| 0192-0193 | F242 | 2016 Jul 20 | 14:39:45.4 | 43015–43021 | 62.6 |
| 0194 | F111 | 2016 Jul 20 | 14:42:59.8 | 43006 | 55.3 |
| 0195 | F111 | 2016 Jul 20 | 14:44:06.6 | 43006–43011 | 55.3 |
| 0196 | F111 | 2016 Jul 20 | 14:45:32.7 | 43010–43013 | 55.3 |
| 0197 | F111 | 2016 Jul 20 | 14:46:39.3 | 43008–43010 | 55.3 |
| 0198 ^a | F111 | 2016 Jul 20 | 14:50:58.4 | 43017–43018 | 55.3 |
| 0199 | F111 | 2016 Jul 20 | 14:53:04.3 | 43017–43018 | 55.3 |
| 0200 | F111 | 2016 Jul 20 | 14:54:11.2 | 43018–43019 | 55.3 |
| 0201-0338 | G227 | 2016 Jul 20 | 14:55:54.3 | 43017–43031 | 4496.7 |
| 0287-0329 | G111 | 2016 Jul 20 | 16:23:39.7 | 43017–43031 | 2010.5 |
| <u>HD 113766</u> | | | | | |
| 0084-0089 | F111 | 2017 Aug 3 | 09:52:55.1 | 38015–38022 | 167.2 |
| 0090-0091 | F242 | 2017 Aug 3 | 09:58:33.9 | 38010–38020 | 44.9 |
| 0092 | F111 | 2017 Aug 3 | 10:00:31.0 | 38014–38019 | 18.6 |
| 0193 | F111 | 2017 Aug 3 | 10:00:57.4 | 38015–38016 | 18.6 |
| 0096-0127 | G111 | 2017 Aug 3 | 10:02:54.7 | 38013–39002 | 1560.5 |
| 0010 | F111 | 2017 Aug 6 | 09:16:30.4 | 37085–37079 | 18.9 |
| 0011 | F111 | 2017 Aug 6 | 09:16:56.4 | 37068–37079 | 18.9 |
| 0014-0077 | G227 | 2017 Aug 6 | 09:19:02.3 | 37110–38095 | 3098.8 |

Notes.

^a No source was found; not used for further analysis.

ORCID iDs

Kate Y. L. Su  <https://orcid.org/0000-0002-3532-5580>
 George H. Rieke  <https://orcid.org/0000-0003-2303-6519>
 Carl Melis  <https://orcid.org/0000-0001-9834-7579>
 Alan P. Jackson  <https://orcid.org/0000-0003-4393-9520>
 Paul S. Smith  <https://orcid.org/0000-0002-5083-3663>
 Huan Y. A. Meng  <https://orcid.org/0000-0003-0006-7937>
 András Gáspár  <https://orcid.org/0000-0001-8612-3236>

References

- Arnold, J. A., Weinberger, A. J., Videen, G., & Zubko, E. S. 2019, *AJ*, **157**, 157
- Baba, H., Yasuda, N., Ichikawa, S.-I., et al. 2002, *RNAOJ*, **6**, 23
- Balling, N. P., Rieke, G. H., Su, K. Y. L., & Gáspár, A. 2017, *ApJ*, **845**, 120
- Balog, Z., Kiss, L. L., Vinkó, J., et al. 2009, *ApJ*, **698**, 1989
- Bohlin, R. C., Gordon, K. D., Rieke, G. H., et al. 2011, *AJ*, **141**, 173
- Bouwman, J., Meeus, G., de Koter, A., et al. 2001, *A&A*, **375**, 950
- Chen, C. H., Mamajek, E. E., Bitner, M. A., et al. 2011, *ApJ*, **738**, 122
- Chen, C. H., Patten, B. M., Werner, M. W., et al. 2005, *ApJ*, **634**, 1372
- Chen, C. H., Sargent, B. A., Bohac, C., et al. 2006, *ApJS*, **166**, 351
- Chen, C. H., Su, K. Y. L., & Xu, S. 2020, *NatAs*, **4**, 328
- Cutri, R. M. 2014, *yCat*, **2328**
- de Vries, B. L., Skogby, H., Waters, L. B. F. M., & Min, M. 2018, *Icar*, **307**, 400
- Ebel, D. S. 2006, in *Meteorites and the Early Solar System II*, ed. D. S. Lauretta & H. Y. McSween (Tucson, AZ: Univ. Arizona Press), 253
- Engler, N., Schmid, H. M., Quanz, S. P., Avenhaus, H., & Bazzon, A. 2018, *A&A*, **618**, A151
- Fabrizius, C., & Makarov, V. V. 2000, *A&A*, **356**, 141
- Fujiwara, H., Onaka, T., Yamashita, T., et al. 2012, *ApJL*, **749**, L29
- Gaia Collaboration, Brown, A. G. A., Vallenari, A., et al. 2018, *A&A*, **616**, A1
- Gaia Collaboration, Prusti, T., de Bruijne, J. H. J., et al. 2016, *A&A*, **595**, A1
- Grady, C. A., Brown, A., Welsh, B., et al. 2018, *AJ*, **155**, 242
- Herter, T. L., Adams, J. D., De Buizer, J. M., et al. 2012, *ApJL*, **749**, L18
- Holden, F. 1976, *PASP*, **88**, 52
- Hughes, A. M., Duchêne, G., & Matthews, B. C. 2018, *ARA&A*, **56**, 541
- Jackson, A. P., & Wyatt, M. C. 2012, *MNRAS*, **425**, 657
- Jackson, A. P., Wyatt, M. C., Bonsor, A., & Veras, D. 2014, *MNRAS*, **440**, 3757
- Johnson, B. C., Lisse, C. M., Chen, C. H., et al. 2012, *ApJ*, **761**, 45
- Johnson, B. C., & Melosh, H. J. 2012, *Icar*, **217**, 416
- Kataza, H., Okamoto, Y., Takubo, S., et al. 2000, *Proc. SPIE*, **4008**, 1144
- Kemper, F., Vriend, W. J., & Tielens, A. G. G. M. 2004, *ApJ*, **609**, 826
- Kennedy, G. M., & Wyatt, M. C. 2013, *MNRAS*, **433**, 2334
- Kessler-Silacci, J., Augereau, J.-C., Dullemond, C. P., et al. 2006, *ApJ*, **639**, 275
- Kiefer, F., Lecavelier des Etangs, A., Augereau, J. C., et al. 2014, *A&A*, **561**, L10
- Kochanek, C. S., Shappee, B. J., Stanek, K. Z., et al. 2017, *PASP*, **129**, 104502
- Koike, C., Noguchi, R., Chihara, H., et al. 2013, *ApJ*, **778**, 60
- Kral, Q., Thébault, P., Augereau, J.-C., Boccaletti, A., & Charnoz, S. 2015, *A&A*, **573**, A39
- Krivov, A. V. 2010, *RAA*, **10**, 383
- Lauretta, D. S., & McSween, H. Y. 2006, *Meteorites and the Early Solar System II* (Tucson, AZ: Univ. Arizona Press)
- Lawler, S. M., Beichman, C. A., Bryden, G., et al. 2009, *ApJ*, **705**, 89
- Lebouteiller, V., Barry, D. J., Spoon, H. W. W., et al. 2011, *ApJS*, **196**, 8
- Lieman-Sifry, J., Hughes, A. M., Carpenter, J. M., et al. 2016, *ApJ*, **828**, 25
- Liou, J. C., & Malhotra, R. 1997, *Sci*, **275**, 375
- Lisse, C. M., Chen, C. H., Wyatt, M. C., & Morlok, A. 2008, *ApJ*, **673**, 1106
- Lisse, C. M., Chen, C. H., Wyatt, M. C., et al. 2009, *ApJ*, **701**, 2019
- Lisse, C. M., Meng, H. Y. A., Sitko, M. L., et al. 2020, *ApJ*, **894**, 116
- MacGregor, A. M., Osten, R. A., & Hughes, A. M. 2020, *ApJ*, **891**, 80
- Mamajek, E. E., & Bell, C. P. M. 2014, *MNRAS*, **445**, 2169
- Marton, G., Calzoletti, L., Perez Garcia, A. M., et al. 2017, arXiv:1705.05693
- Mathews, B. C., Krivov, A. V., Wyatt, M. C., Bryden, G., & Eiroa, C. 2014, in *Protostars and Planets VI*, ed. H. Beuther et al. (Tucson, AZ: Univ. Arizona Press), 521
- Melis, C. 2016, in *IAU Symp. 314, Young Stars & Planets Near the Sun*, ed. J. H. Kastner, B. Stelzer, & S. A. Metchev (Cambridge: Cambridge Univ. Press), 241
- Melis, C., Zuckerman, B., Rhee, J. H., et al. 2012, *Natur*, **487**, 74
- Melis, C., Zuckerman, B., Rhee, J. H., et al. 2013, *ApJ*, **778**, 12
- Melis, C., Zuckerman, B., Rhee, J. H., & Song, I. 2010, *ApJL*, **717**, L57
- Meng, H. Y. A., Rieke, G. H., Su, K. Y. L., & Gáspár, A. 2017, *ApJ*, **836**, 34
- Meng, H. Y. A., Su, K. Y. L., Rieke, G. H., et al. 2014, *Sci*, **345**, 1032
- Meng, H. Y. A., Su, K. Y. L., Rieke, G. H., et al. 2015, *ApJ*, **805**, 77
- Meyer, M. R., Backman, D., Mamajek, E. E., et al. 2001, *AAS Meeting*, **199**, 76.08
- Mittal, T., Chen, C. H., Jang-Condell, H., et al. 2015, *ApJ*, **798**, 87
- Morlok, A., Mason, A. B., Anand, M., et al. 2014, *Icar*, **239**, 1
- Okamoto, Y. K., Kataza, H., Yamashita, T., et al. 2003, *Proc. SPIE*, **4841**, 169
- Olofsson, J., Henning, T., Nielbock, M., et al. 2013, *A&A*, **551**, A134
- Olofsson, J., Juhász, A., Henning, T., et al. 2012, *A&A*, **542**, A90
- Osten, R., Livio, M., Lubow, S., et al. 2013, *ApJL*, **765**, L44
- Pecaut, M. J., Mamajek, E. E., & Bubar, E. J. 2012, *ApJ*, **746**, 154
- Rebull, L. M., Stapelfeldt, K. R., Werner, M. W., et al. 2008, *ApJ*, **681**, 1484
- Rhee, J. H., Song, I., & Zuckerman, B. 2008, *ApJ*, **675**, 777
- Rieke, G. H., Blaylock, M., Decin, L., et al. 2008, *AJ*, **135**, 2245
- Riviere-Marichalar, P., Barrado, D., Montesinos, B., et al. 2014, *A&A*, **565**, A68
- Sargent, B. A., Forrest, W. J., Tayrien, C., et al. 2009, *ApJS*, **182**, 477
- Schütz, O., Meeus, G., & Sterzik, M. F. 2005, *A&A*, **431**, 175
- Sierchio, J. M., Rieke, G. H., Su, K. Y. L., & Gáspár, A. 2014, *ApJ*, **785**, 33
- Smith, R., Wyatt, M. C., & Haniff, C. A. 2012, *MNRAS*, **422**, 2560
- Song, I., Zuckerman, B., Weinberger, A. J., & Becklin, E. E. 2005, *Natur*, **436**, 363
- Su, K. Y. L., Jackson, A. P., Gáspár, A., et al. 2019, *AJ*, **157**, 202
- Su, K. Y. L., Morrison, S., Malhotra, R., et al. 2015, *ApJ*, **799**, 146
- Su, K. Y. L., & Rieke, G. H. 2014, in *IAU Symp. 299, Exploring the Formation and Evolution of Planetary Systems*, ed. M. Booth, B. C. Matthews, & J. R. Graham (Cambridge: Cambridge Univ. Press), 318
- Thebault, P., & Kral, Q. 2019, *A&A*, **626**, A24
- Thompson, M. A., Weinberger, A. J., Keller, L. D., Arnold, J. A., & Stark, C. C. 2019, *ApJ*, **875**, 45
- Torres, C. A. O., Quast, G. R., da Silva, L., et al. 2006, *A&A*, **460**, 695
- van Dishoeck, E. F. 2004, *ARA&A*, **42**, 119
- Weinberger, A. J., Becklin, E. E., Song, I., & Zuckerman, B. 2011, *ApJ*, **726**, 72
- Wyatt, M. C. 2008, *ARA&A*, **46**, 339
- Wyatt, M. C., Smith, R., Greaves, J. S., et al. 2007, *ApJ*, **658**, 569
- Zellner, N. E. B. 2019, *JGRE*, **124**, 2686